Misfit-dislocation hierarchy governs sliding of asymmetric non-CSL grain boundaries

Kunqing Ding[1,+], Yazhuo Liu[1,+], Yin Zhang[2], Lihua Wang[3], Xiaodong Han[3], Ting Zhu[1,*]

[1]Woodruff School of Mechanical Engineering, Georgia Institute of Technology, Atlanta, Georgia 30332, USA

[2]School of Mechanics and Engineering Science, Peking University, 100871, Beijing, China

[3]Institute of Microstructure and Property of Advanced Materials, Beijing Key Lab of Microstructure and Property of Advanced Materials, Beijing University of Technology, Beijing, 100124, China

Abstract

Grain boundary (GB) deformation significantly influences the mechanical response of polycrystalline materials, yet most atomistic studies have focused on coincidence site lattice (CSL) boundaries. Motivated by in situ atomic-resolution observations, we investigate step-free sliding along asymmetric non-CSL tilt GBs in face-centered cubic (FCC) metals using atomistic modeling. In these incommensurate GBs, a dense array of primary misfit dislocations accommodates the local interfacial mismatch, whereas a more widely spaced array of secondary GB misfit dislocations accommodates the residual mismatch. Uniform sliding calculations reveal two distinct quantities: the minimum GB structural periodicity $\boldsymbol{\lambda}$, defined by the repeating arrangement of primary GB misfit dislocations, and the slip vector $\mathbf{b}$, determined by the minimum displacement-shift-complete translation that restores an equivalent GB structure. Nonuniform sliding proceeds through the glide of secondary GB misfit dislocations, which carry $\mathbf{b}$ and transform successive boundary segments between crystallographically equivalent translation states. These secondary misfit dislocations dissociate into partials, each carrying a partial Burgers vector $\mathbf{b_p}$ and connecting intermediate interfacial states. The characteristic spacing between secondary misfit partials defines a longer periodicity $\boldsymbol{\Lambda}$. Below the athermal stress, each partial glides through a two-step thermally activated kink-pair mechanism, advances the partial by one structural period $\boldsymbol{\lambda}$. These results establish a unified crystallographic and dislocation-based framework for understanding stress-driven sliding in structurally complex asymmetric GBs.

*Corresponding author: ting.zhu@me.gatech.edu

[+]These authors contribute equally.

1. Introduction

Grain boundaries (GBs) separate adjacent grains in polycrystalline materials and strongly influence yield strength, tensile ductility, creep resistance, and fracture toughness [1]. In fine-grained and nanocrystalline metals, the substantial GB volume fraction can make GB-mediated plasticity the dominant deformation mode [2]. Although atomic-scale microscopy and modeling have significantly advanced the understanding of GB structure and behavior [3-10], most studies have focused on coincidence site lattice (CSL) GBs [11, 12], particularly symmetric tilt GBs [13], because of their relatively simple crystallography and computational tractability [14].

Recent experimental and theoretical studies have extended the understanding of GB deformation from ideal symmetric boundaries to structurally complex GBs. Dislocation- and disconnection-based descriptions establish that interfacial line defects can accommodate both relative grain translation and shear-coupled boundary migration [6, 15-17]. Attention has also shifted toward asymmetric non-CSL GBs, many of which are incommensurate [16-22]. For example, high resolution transmission electron microscopy (HRTEM) has revealed the atomic structures of 90° ⟨110⟩ tilt GBs, while atomistic modeling has indicated inclination-dependent sliding resistances in {100}/{110} and {111}/{112} boundaries [23, 24]. Subsequent in situ nanomechanical experiments demonstrated nearly frictionless sliding along these asymmetric incommensurate GBs [25]. Despite these advances, the crystallographic origins and thermally activated kinetic behavior of step-free sliding in asymmetric non-CSL GBs remain less well understood.

Engineering polycrystals contain predominantly asymmetric non-CSL GBs. In face-centered cubic (FCC) materials, asymmetric non-CSL tilt GBs containing at least one low-index terminating plane, such as {111} or {100}, are frequently observed [8, 9, 26-29]. Under applied stress, such boundaries can undergo sliding that is mediated by step-free GB dislocations [8] rather than by the commonly studied step-bearing disconnections. This distinction raises several fundamental questions. What determines the structural periodicity of these complex interfaces? What is the minimum relative displacement between adjacent grains, represented by a displacement-shift-complete (DSC) translation [1], that restores an equivalent GB structure? How is this structure-preserving translation localized and propagated by GB dislocations during stress-driven sliding?

To address these questions, we use atomistic modeling of FCC Ni bicrystals to characterize stress-driven sliding in asymmetric non-CSL tilt GBs. The study is motivated by in situ atomic-resolution experiments by Wang et al. [8], who directly observed GB dislocation motion during sliding-dominated deformation. We examine asymmetric ⟨110⟩ tilt GBs containing at least one low-index terminating plane, including {331}/{111}, {100}/{111} and {100}/{110}. In these incommensurate boundaries, the ratio of the surface lattice repeat distances along the sliding direction is irrational, producing interfacial mismatch across two characteristic length scales. A dense array of primary misfit dislocations accommodates the local mismatch, whereas a more widely spaced array of secondary misfit dislocations accommodates the residual mismatch relative to a near-CSL reference. Uniform sliding calculations are used to determine the minimum structural period $\boldsymbol{\lambda}$ and the structure-preserving slip vector $\mathbf{b}$, which are generally distinct in complex GBs [3]. We find that primary misfit dislocations undergo only local rearrangement and are effectively non-glissile. By contrast, secondary GB misfit dislocations propagate over multiple structural periods and carry $\mathbf{b}$, thereby mediating nonuniform GB sliding. Notably, these secondary GB misfit dislocations dissociate into partials with Burgers vector $\mathbf{b_p}$. In a relaxed extended boundary, sparsely distributed secondary misfit partials recur with a longer characteristic spacing $\boldsymbol{\Lambda}$. The partials glide through a localized kink-pair mechanism below the athermal stress. These results demonstrate how a hierarchy of primary and secondary misfit dislocations dictates the structural defects and sliding behavior in asymmetric non-CSL GBs.

2. Model and results

2.1 Simulation methods

All atomistic simulations were performed using LAMMPS [30], and atomic configurations were visualized using OVITO [31]. Asymmetric ⟨110⟩ tilt GBs were constructed in FCC Ni bicrystals by orienting two crystals with a common ⟨110⟩ tilt axis and joining them along the prescribed GB planes. For each bicrystal, the relative translation between the grains was varied, and the resulting structures were relaxed by conjugate gradient energy minimization to identify the lowest-energy interfacial configuration among the sampled translations for subsequent sliding calculations. Periodic boundary conditions were applied along the out-of-plane tilt-axis direction. The lateral, upper, and lower surfaces were traction-free during GB relaxation.

The Pt GBs observed experimentally by Wang et al. [8] provide the structural and mechanistic motivation for this study. However, the currently available classical Pt potentials that we examined did not reproduce atomic GB structures that agree with these observations. The angular-dependent potential (ADP) for Ni developed by Howells et al. [32] reproduced the relevant experimental GB structural motifs and was therefore used as the model potential for an FCC metal. The quantitative dislocation-core structures and energy barriers reported below are specific to this Ni potential. Nevertheless, the crystallographic characteristics of structure-preserving GB translation states identified in the Ni simulations are expected to apply more broadly to FCC metals.

Relaxed GB structures were used to determine the GB structural periodicity $\boldsymbol{\lambda}$ from the repeating arrangement of primary GB misfit dislocations, which were identified by extra half-plane terminations at GBs. Uniform GB sliding was simulated by applying successive shear displacement increments through the top and bottom boundary layers. The upper grain was displaced relative to the lower grain in increments parallel to the GB plane. After each increment, the bicrystal was relaxed by conjugate gradient energy minimization while maintaining the imposed displacement at the external boundary layers. The resulting sequence of relaxed configurations was used to identify crystallographically equivalent GB translation states and to determine the Burgers vectors of the full and partial GB misfit dislocations, $\mathbf{b}$ and $\mathbf{b}_p$. We stress that because the partial dislocations connect intermediate GB states involving substantial relative displacements between atomic columns at the boundary, their Burgers vectors $\mathbf{b}_p$ cannot be inferred solely from the DSC lattice generated by rigid relative translations of adjacent grains. Instead, nearest-neighbor atom pairs across the GB were tracked to construct relative-displacement maps and calculate cumulative sliding displacements, from which $\mathbf{b}$ and $\mathbf{b}_p$ were determined.

Secondary GB misfit dislocations were introduced by spatially localizing the structure-preserving translation identified from the uniform-sliding calculations. Because the secondary GB misfit dislocation dissociates into partial dislocations, a leading GB misfit partial was first introduced by imposing a relative displacement equal to its partial Burgers vector between atom pairs across the GB on one side of the intended dislocation core. Structural relaxation then produced a localized interfacial translation. The transition region between the states with and without translation defines the core of the GB misfit partial dislocation. A second GB misfit partial

was then introduced similarly to reveal the resulting structure and interaction between the two partials.

Thermally activated glide of the GB misfit partial dislocation was characterized using the stress-controlled nudged elastic band (σ-NEB) method [33]. A constant force parallel to the GB was applied to atoms in the upper five atomic layers, while atoms in the lower five layers were fixed. This arrangement imposed the prescribed shear stress during relaxation. The initial and final states were neighboring local energy minima separated by one elementary propagation event of the GB partial dislocation. Intermediate NEB images were generated by linearly interpolating between the initial and final configurations and subsequently relaxed using the QuickMin algorithm.

Two σ-NEB model geometries were used. In the quasi-two-dimensional (2D) model, the bicrystal thickness along the ⟨110⟩ tilt axis was approximately 1 nm. This constraint caused equivalent atomic columns along the tilt-axis direction to undergo nearly identical displacements, thereby enabling resolution of the elementary glide pathway and intermediate metastable states. To examine spatially localized, thermally activated processes, the bicrystal was extended along the tilt-axis direction, yielding a three-dimensional (3D) model. The 3D σ-NEB calculations allowed the GB dislocation line to move nonuniformly along its length, enabling localized kink-pair formation and migration.

2.2 Structure of asymmetric tilt GBs

We focused on an asymmetric non-CSL tilt GB in an FCC Ni bicrystal. Its structure closely resembles that of the FCC Pt GB observed by Wang et al. [8] using in situ nanomechanical testing with HRTEM. Figs. 1a-1c show the atomic structure of the asymmetric ⟨110⟩ tilt GB with a misorientation of 21.8° after conjugate gradient energy minimization. Grains G1 and G2 are aligned along the $[\bar{1}10]$ zone axis. Grain G1 terminates at a high-index (331) surface, whereas grain G2 terminates at a flat close-packed (111) surface. The bicrystal measures 13 × 18 × 1 nm^3 and contains 21,812 atoms. For comparison, Figs. 1d-1f present HRTEM images of the analogous experimental GB [8]. The two grains are aligned along the $[\bar{1}10]$ zone axis, and each white spot represents a projected $[\bar{1}10]$ atomic column. Grain G1 exposes a high-index (331) surface with single-atom-height steps separated by short (111) and $(1\bar{1}1)$ facets (marked in Fig. 1d), whereas grain G2 exposes a flat close-packed (111) surface. This configuration constitutes an asymmetric

non-CSL tilt GB and differs from the CSL boundaries commonly considered in atomistic simulations.

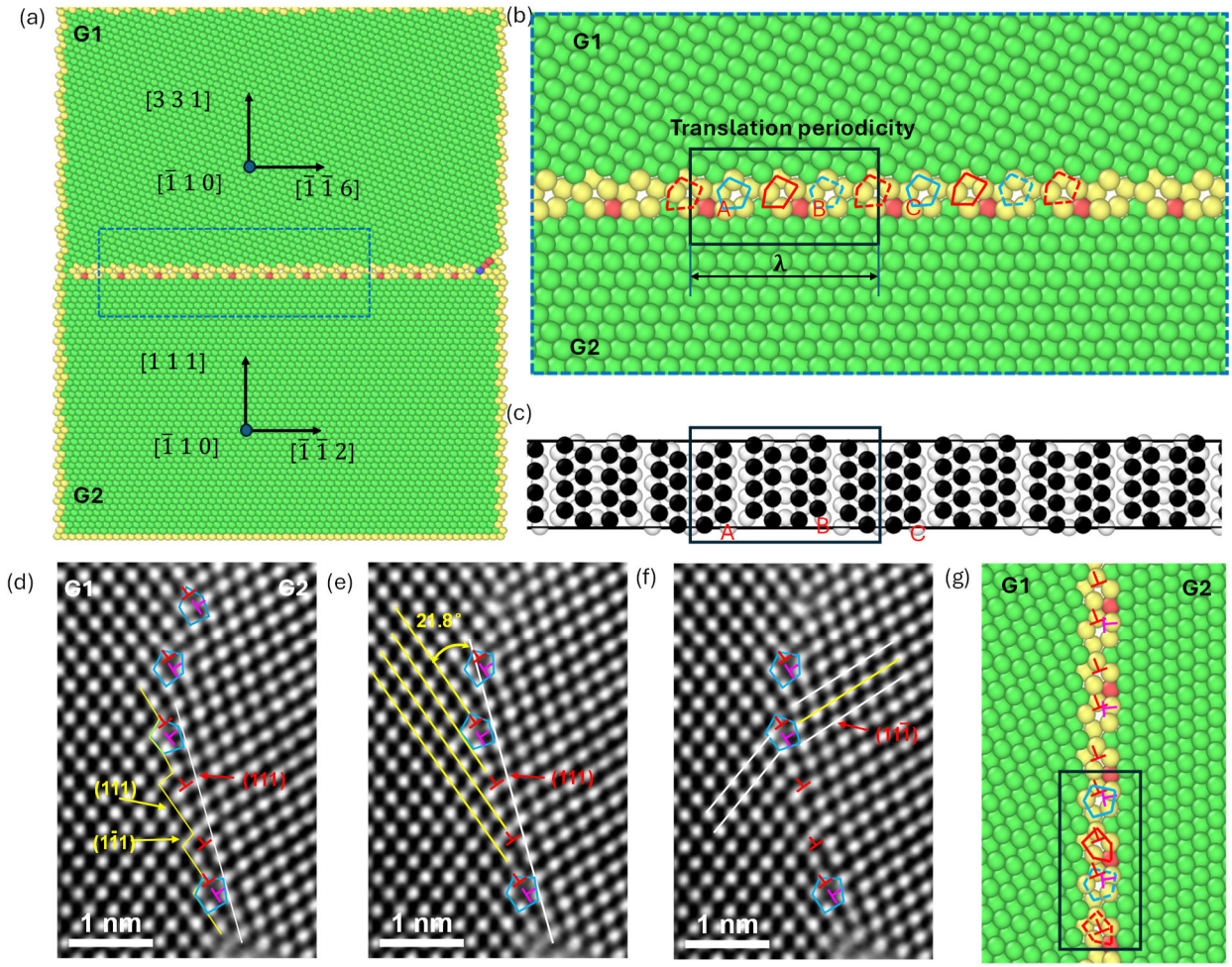

Fig. 1. Structure of an asymmetric non-CSL ⟨110⟩ tilt GB with a misorientation of 21.8°. (a) Atomic configuration of the Ni bicrystal, where grain G1 terminates at a (331) surface and grain G2 terminates at a flat close-packed (111) surface. Atoms are colored by common neighbor analysis: FCC (green), hexagonal close-packed (HCP, red), and others (yellow). (b) Enlarged view of the boxed region in (a). The structural period **λ** (solid box) spans four distinct pentagon-shaped structural units (outlined with different line colors and types). (c) Top-down view showing only grain surface atoms: G1 (black) and G2 (white). The out-of-plane registry for atoms A, B, and C (labeled in (a)) is shown along the [$\bar{1}$10] direction. (d) HRTEM image of an analogous GB in a Pt bicrystal, adapted from Wang et al. [8]. G1 contains a high-index (331) surface with single-atom-height steps separated by short (111) and (1$\bar{1}$1) facets (yellow lines), while G2 terminates at a flat (111) grain surface (white line). (e, f) The same HRTEM image as (d), with yellow lines indicating extra half-planes associated with misorientation dislocations in (e) and a misfit dislocation in (f). Red ⊥ symbols identify the terminations of extra half-planes and thus the cores of misorientation dislocations. Pink ⊥ symbols identify the cores of misfit dislocations. (g) Atomic GB model

annotated over one structural period (solid box), showing both pentagon units and the corresponding GB dislocations.

To determine the GB structural periodicity, we analyzed the structural units within the boxed region of Fig. 1a (detailed in Fig. 1b). Although the projected boundary structure appears to contain alternating regular (blue) and distorted (red) pentagon units in Fig. 1b, these 2D profiles do not define the complete periodicity because they omit the 3D interfacial registry. Fig. 1c presents a top-down view of the surface atoms in G1 (black) and G2 (white), revealing their relative registry along the $[\bar{1}10]$ zone axis. The G1 atoms occupy three-fold hollow sites above the close-packed (111) surface of G2. Atoms A and C have identical out-of-plane positions, whereas atom B is displaced to occupy a different out-of-plane position. As a result, the blue pentagon units associated with atoms A and B possess distinct 3D configurations, despite their similar projected profiles. The smallest complete structural repeat therefore contains four crystallographically distinct pentagon units (distinguished by color and line style in Fig. 1b). This repeat defines a structural period $\boldsymbol{\lambda}$ of $5/2[\bar{1}\bar{1}2](111)$ relative to the G2 lattice, with a magnitude of ~ 2.2 nm.

What structural factors govern the structural periodicity along an asymmetric non-CSL tilt GB? The periodicity is defined by the smallest repeating motif of primary misfit dislocations, characterized by their spacing and sequence along the interface. Specifically, in the experimental GB shown in Figs. 1d-1f, two interfacial features are interpreted as primary GB dislocations. The first accommodates lattice misorientation and has a Burgers vector of $1/2[110]$; it is marked by a red $\perp$ symbol at the termination of an extra half (111) plane indicated by a yellow line in Fig. 1e. The second accommodates interfacial misfit and thus is the primary GB misfit dislocation with a Burgers vector of $1/2[01\bar{1}]$; it is marked by a pink $\perp$ symbol at the termination of an extra half $(1\bar{1}1)$ plane indicated by a yellow line in Fig. 1f. These dislocations frequently pair to form a GB Lomer lock. As shown in Fig. 1J of Ref. [8], Burgers circuit analysis identified a combined Burgers vector $1/2[101]$ of the lock, corresponding to $1/2[110] + 1/2[0\bar{1}1]$. In Figs. 1d-1f, the core of a GB Lomer lock appears as a regular pentagon, whereas that of an isolated misorientation dislocation appears as a distorted pentagon. This experimental GB is not perfectly periodic because it contains a (331) surface step [8]. In contrast, the model in Fig. 1g contains no such step and therefore isolates sliding in a flat boundary. It reveals a repeating sequence of alternating GB

Lomer locks and misorientation dislocations. The structural periodicity is determined by the spacing between successive equivalent pentagons. This periodicity is consistent with the out-of-plane atomic registry discussed earlier.

The assignment of individual primary GB dislocations in the experimental HRTEM images should be interpreted cautiously. Figs. 1d–1f directly reveal atomic-column arrangements, extra half-planes, and variations in interfacial structural units. The misorientation and misfit dislocations, denoted by the red and pink $\perp$ symbols, are assigned based on the terminations of extra half-planes and comparison with the corresponding atomistic model. This comparison is necessary because each white spot in the HRTEM image represents a projected atomic column, which can occupy one of two distinct positions along the out-of-plane $[\bar{1}10]$ direction, as discussed earlier. The experimental images alone therefore do not uniquely determine the 3D interfacial defect structure. The misorientation and misfit dislocations, together with the structural periodicity $\boldsymbol{\lambda}$ used in the subsequent analysis, are determined from the fully resolved atomistic model rather than from the experimental defect assignments alone.

2.3 Uniform GB sliding

Using the bicrystal model in Fig. 1a, we investigated uniform GB sliding by applying incremental in-plane shear displacements to the upper surface relative to the lower surface, followed by relaxation via conjugate gradient energy minimization after each increment. This calculation provides a direct means to identify the structure-preserving translation and the corresponding slip vector **b** of the GB. Fig. 2a presents a magnified view of the GB region during uniform sliding, illustrating the leftward translation of grain G1 relative to G2. Structural analysis reveals that a full DSC translation is achieved through four discrete sliding steps. Figs. 2b1-2b5 display the top-down relative displacement maps for nearest-neighbor atom pairs across the GB at each step. Fig. 2b5 repeats Fig. 2b1, confirming that a complete structural shift is reached after the four-step sequence shown in Figs. 2b1-2b4. Within each map, neighboring atomic columns (brown box) exhibit identical relative displacements; four such column pairs constitute a single periodic unit (black box), consistent with the structural periodicity identified in Fig. 1b. In Figs. 2b1-2b4, the average relative displacement within each periodic unit is approximately $1/8[\bar{1}\bar{1}2](111)$ relative to the G2 lattice. Fig. 2b6 displays the cumulative relative displacement map for all nearest-neighbor atom pairs across the GB; minor deviations from the exact lattice period

$1/2[\bar{1}\bar{1}2](111)$ arise from elastic deformation caused by the applied shear loading. Therefore, the slip vector for this asymmetric GB is determined to be $\mathbf{b} = 1/2[\bar{1}\bar{1}2](111)$, which is realized via four sequential increments (Figs. 2b1-2b4), each involving a partial slip vector of $\mathbf{b}_p = 1/8[\bar{1}\bar{1}2](111)$.

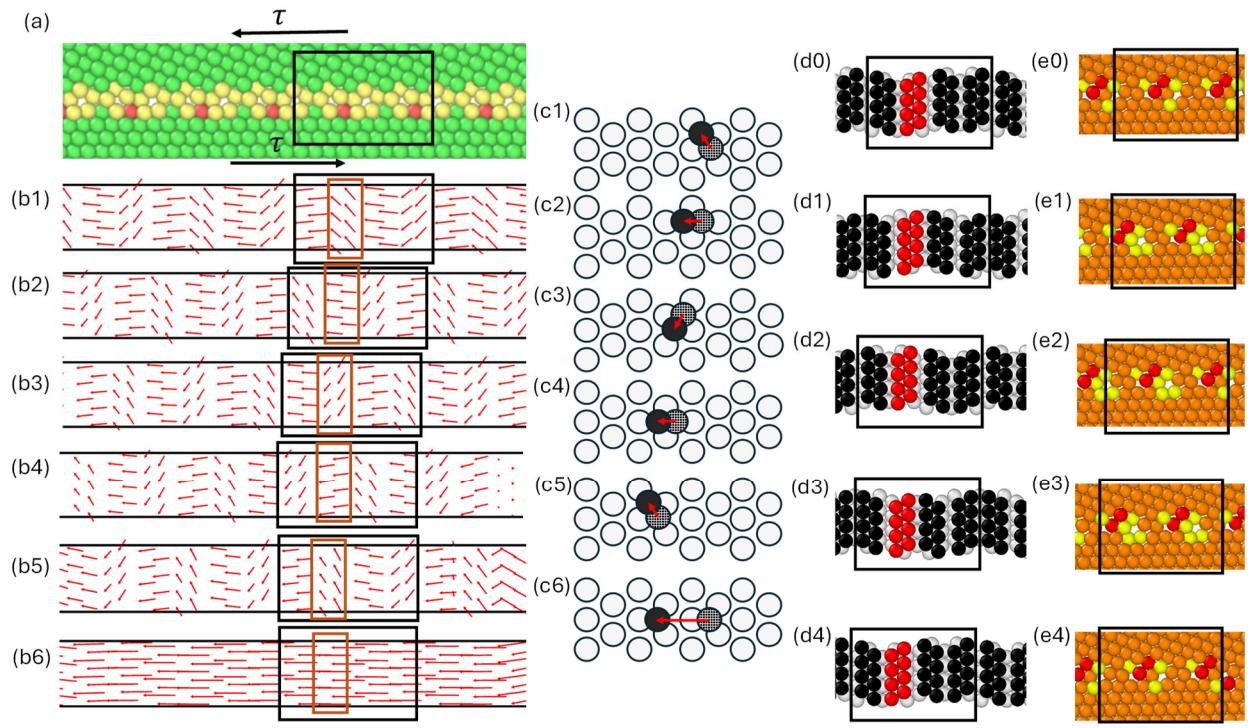

Fig. 2. Uniform GB sliding under applied shear stress τ. (a) Magnified view of the GB region, with one structural period indicated by a solid box. Atoms are colored by common neighbor analysis. (b) Top-down relative displacement maps for nearest-neighbor atom pairs across the GB during four sequential sliding steps (b1-b4). The map in (b5) repeats (b1), confirming that a DSC translation is achieved after the four steps. (b6) shows the cumulative relative displacement map obtained by summing (b1-b4). (c) Schematics of a representative G1 surface atom progressing through four sequential sliding steps (c1-c4) to reach the DSC state (c5). The cumulative relative displacement of this atom is illustrated in (c6). (d) Top-down positions of G1 and G2 surface atoms before and after each sliding step (d0-d4). (e) $[\bar{1}10]$ views of the corresponding GB structures in (d). Atoms are colored by coordination number N: 12 (orange, perfect FCC structure), 13 (red), and 11 (yellow).

What determines the slip vector of an asymmetric tilt GB during sliding without migration? In asymmetric tilt GBs containing a flat close-packed (111) grain surface, the slip vector is governed by the lattice periodicity of the (111) surface in the sliding direction [3]. Each surface atom of grain G1 traverses four sequential steps to achieve a DSC translation of $1/2[\bar{1}\bar{1}2](111)$, a vector

consistent with the in-plane lattice periodicity of the G2 (111) surface. Figs. 2c1-2c4 illustrate a G1 surface atom moving in $1/6\langle 112\rangle$ increments between three-fold hollow sites (indicated by gridded to solid circles) atop the G2 (111) plane. After four steps, the atom returns to an equivalent site (Fig. 2c5). The total relative displacement (Fig. 2c6) confirms a cumulative slip vector **b** of $1/2[\bar{1}\bar{1}2](111)$. Each incremental step of an atomic column corresponds to a specific variant of the $1/6\langle 112\rangle$ family, and neighboring atomic columns within a single GB periodic unit follow different $1/6\langle 112\rangle$ variants. Nonetheless, the cumulative slip vector of $1/2[\bar{1}\bar{1}2](111)$ remains dictated by the G2 (111) lattice periodicity.

Top-down views of the G1 and G2 surface atoms during these four sliding steps are shown in Figs. 2d0-2d4. By Fig. 2d4, the atomic pattern within the GB periodic unit (black box) repeats that in Fig. 2d0 but is translated leftward by **b**, confirming the DSC translation. Figs. 2e0-2e4 present $[\bar{1}10]$ views of the same steps shown in Figs. 2d0-2d4, with atoms colored by coordination number. In Fig. 2e4, the periodic unit (black box) likewise repeats that in Fig. 2e0 with a shift of **b**. Intermediate states (Figs. 2e1-2e3) exhibit an increase in miscoordinated atoms resulting from partial slips of $\mathbf{b}_p$. After the fourth step, the total sliding displacement of **b** restores the initial structure (Fig. 2e4). These miscoordinated atoms are primarily localized to the G1 and G2 surface layers (Figs. 2e1-2e3), where atoms undergo significant relative displacements; conversely, atoms within the grain interiors experience minimal rigid-body shifts of $\mathbf{b}_p$ per step.

The uniform-sliding calculation characterizes the interfacial translation landscape and does not imply that an extended GB must slide coherently along its entire length. The initial and final configurations separated by DSC vector **b** are crystallographically equivalent translation states of the same GB. In an extended GB, this structure-preserving translation can be spatially localized. Adjacent GB segments may occupy the two translation states, with the line defect separating them constituting a secondary GB misfit dislocation with Burgers vector **b**. As this defect propagates, it progressively transforms the boundary segment from one translation state to the other, thereby producing nonuniform GB sliding without requiring simultaneous translation of the entire interface. This dislocation-mediated nonuniform sliding generally requires a lower driving stress than uniform sliding. The uniform-sliding pathway therefore provides a crystallographic basis for the subsequent study of GB-dislocation-mediated nonuniform sliding.

2.4 Motion of secondary GB misfit dislocations

We examined the localized dislocation-mediated counterpart to the uniform sliding process described in Section 2.3. For the asymmetric tilt GB shown in Fig. 1a, a secondary GB misfit dislocation carries the full Burgers vector **b** $=1/2[\bar{1}\bar{1}2](111)$. To produce a structure-preserving translation by **b**, the dislocation must propagate at least one GB structural period $\boldsymbol{\lambda} = 5/2[\bar{1}\bar{1}2](111)$. Thus, **b** defines the relative grain translation carried by the dislocation, whereas $\boldsymbol{\lambda}$ defines the propagation distance to restore an equivalent GB structure. The uniform-sliding results further indicate that the secondary misfit dislocation dissociates into four partials, each carrying a partial Burgers vector $\mathbf{b}_p = \mathbf{b}/4 = 1/8[\bar{1}\bar{1}2](111)$.

Primary and secondary GB misfit dislocations play distinct roles in the sliding process. Primary misfit dislocations are the constituent defect structure of the interface and define its smallest structural periodicity. During the sliding sequence in Fig. 2, they undergo local atomic rearrangements as the boundary is transformed between equivalent translation states. Their cores do not propagate along the GB over distances exceeding one structural period $\boldsymbol{\lambda}$ and are therefore effectively non-glissile within the GB plane. In contrast, a secondary misfit GB dislocation can propagate successively through multiple structural periods. Its glide carries the relative grain translation **b** along the boundary, thereby producing a net sliding displacement. This distinction between locally rearranging primary misfit defects and propagating secondary misfit defects provides the dislocation-based foundation for understanding nonuniform GB sliding.

At finite temperatures, dislocation glide occurs via thermally activated processes when the applied shear stress is below the athermal threshold, at which the energy barrier vanishes and motion becomes instantaneous. To characterize this thermally activated process, we employed the σ-NEB method [33] and first modeled a GB dislocation within a thin bicrystal (~1 nm thick). This setup constrains the dislocation to 2D motion, yielding identical atomic displacements along each $[\bar{1}10]$ column (Figs. 3a-3b). To prepare for the σ-NEB calculation, the leading partial of a secondary GB misfit dislocation was introduced by imposing a relative displacement [34] of $\mathbf{b}_p$ between atom pairs across the GB in Fig. 1a, on the left side of the intended dislocation core, followed by structural relaxation. The resulting core (yellow box in Fig. 3b1) spans about five pentagon units and is composed primarily of miscoordinated atoms. The GB structure trailing the partial dislocation core differs from that ahead of the core, exhibiting variations in atomic

coordination and out-of-plane registry; the atomic configurations of single and double GB partial dislocations will be compared in the Discussion section.

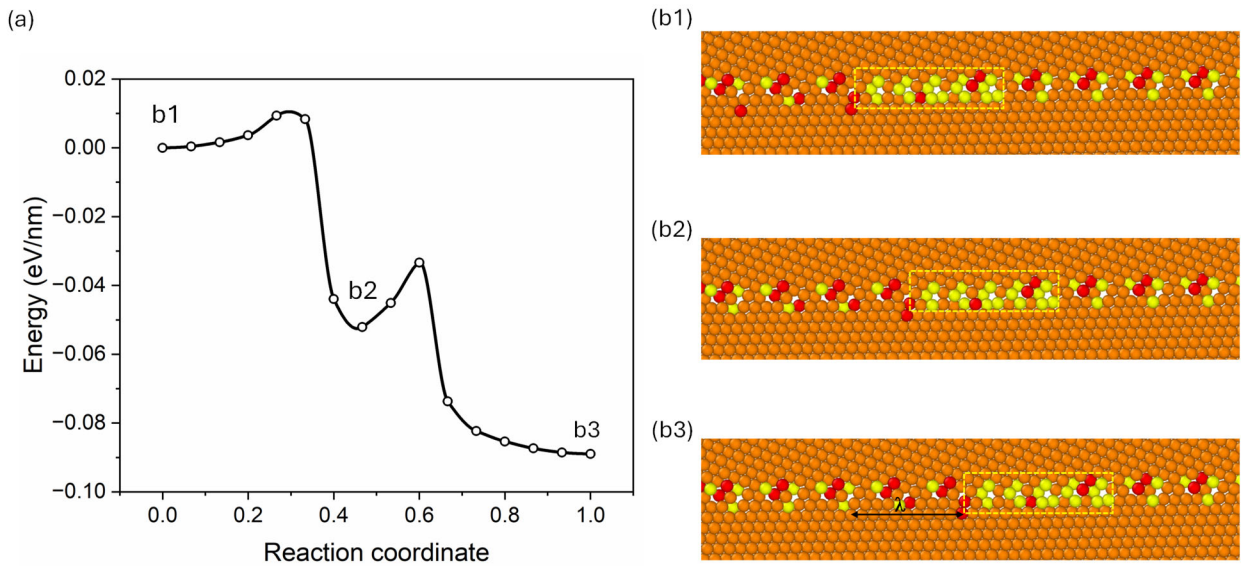

Fig. 3. 2D σ-NEB results for an elementary event of thermally activated glide of the leading partial of a secondary GB misfit dislocation. (a) MEP under an applied shear stress τ of 59.7 MPa. Three local energy minima are labeled b1-b3, indicating that one elementary glide event proceeds through two sequential steps (b1→b2 and b2→b3). (b) Atomic configurations (b1-b3) correspond to these minima in (a). Atoms are colored by coordination number, as in Fig. 2e. The core of the leading partial, highlighted by a yellow dashed box, is composed primarily of miscoordinated (yellow) atoms and moves by one GB structural period λ from (b1) to (b3).

For example, under an applied shear stress τ of 59.7 MPa (below the athermal stress of 165 MPa), the σ-NEB calculation converges to a minimum energy path (MEP) for a single rightward glide event of the secondary GB misfit partial. As shown in Fig. 3a, the MEP reveals that this elementary glide event proceeds via two sequential steps, evidenced by two successive energy barriers and three local minima. The atomic configurations corresponding to these minima are shown in Figs. 3b1-3b3. From the initial to the final state, atom pairs within the partial dislocation core undergo a relative shift equal to the partial Burgers vector $\mathbf{b}_p = 1/8[\bar{1}\bar{1}2](111)$. This results in a rightward core translation by one GB structural period $\lambda = 5/2[\bar{1}\bar{1}2](111)$ (Fig. 3b3). The intermediate local minimum (b2 in Fig. 3a) and its corresponding core configuration in Fig. 3b2 separates the two steps. The first step displaces the core by λ/2, while the second step completes the motion with the remaining λ/2. The stepwise glide mechanism drives nonuniform GB sliding

through repeated glide increments of these secondary GB misfit partials. This result identifies $\lambda/2$ (~ 1.1 nm) as the smallest resolved glide increment of the partial dislocation.

The 2D σ-NEB calculation in Fig. 3a reveals two energy barriers, each scaling linearly with crystal thickness. Because these barriers cannot increase indefinitely with thickness, the glide process is expected to adopt a localized 3D mechanism with lower energy barriers. The 3D σ-NEB calculation identifies a kink-pair mechanism, uncommon in FCC metals [33], that enables the glide of a secondary GB misfit partial in the bicrystal shown in Fig. 1a. The bicrystal was extended along the out-of-plane $[\bar{1}10]$ direction to 17.9 nm, yielding a thicker GB structure with 392,778 atoms. Fig. 4a presents the corresponding MEP under a shear stress of 23.9 MPa. The associated displacements of G1 surface atoms, reflecting the relative displacements across the boundary, are displayed in Figs. 4b1-4b4. As in the 2D σ-NEB case (Fig. 3), the 3D elementary glide event involves two sequential steps, each mediated by a kink pair. In the first step, a kink pair (Fig. 4b1) forms in the dislocation core near the first saddle point (b1 in Fig. 4a). The two kinks migrate in opposite directions until the dislocation restores a straight configuration at an intermediate minimum (Fig. 4b2; b2 in Fig. 4a). The second step follows, with a second kink pair (Fig. 4b3) forming near the second saddle point (b3 in Fig. 4a). This process progresses to the final minimum (b4 in Fig. 4a), again resulting in a straight dislocation core (Fig. 4b4). The saddle points b1 and b3 in Fig. 4a correspond to energy barriers of 0.37 eV and 0.49 eV, respectively. The latter is the rate-limiting barrier and therefore defines the activation energy E_{a} for the overall glide process and, consequently, the kinetics of GB sliding.

Kink-pair formation itself is a well-established mechanism of thermally activated dislocation motion. The significance of the present result is that, for this representative {331}/{111} GB, kink-pair formation and migration involve a distinct rate-controlling atomistic pathway through which a localized GB translation state propagates across the periodic interfacial structure. Our σ-NEB calculations directly characterize the associated energy barrier and reveal a mechanism comprising two sequential kink-pair steps. This mechanism is more complex than the single kink-pair step commonly associated with the elementary glide event of an isolated dislocation in the lattice.

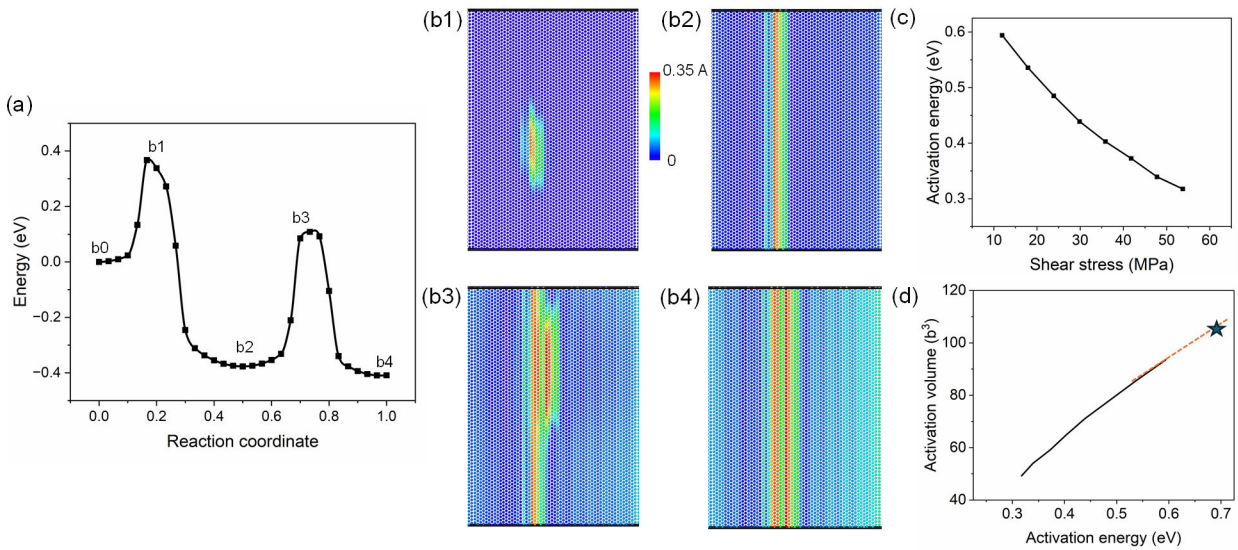

Fig. 4. 3D σ-NEB results for an elementary event of thermally activated glide of the leading partial of a secondary GB misfit dislocation. (a) MEP under an applied shear stress of $\tau = 23.9$ MPa. (b) Contour map of sliding displacement Δd of G1 surface atoms, referenced to the configuration (not shown) at the initial local energy minimum (denoted as b0). The corresponding energies of states b0-b4 are indicated in (a). (c) Activation energy E_a as a function of applied shear stress τ. (d) Activation volume V_a as a function of activation energy E_a. The data are extrapolated to higher E_a values (red dashed line) to obtain the characteristic V_a value (marked by a star) at $E_\mathrm{a} = 0.7$ eV.

We further calculated the activation energy E_a for the kink-pair mechanism across a range of shear stresses τ (Fig. 4c). A characteristic E_a value of 0.7 eV corresponds to a typical laboratory strain rate of 10^{-3} s^{-1} at room temperature [33]. From Fig. 4c, the required τ is less than 10 MPa when $E_\mathrm{a} = 0.7$ eV, indicating that the glide of this GB partial dislocation can be activated under relatively low driving stresses. Because of stability limits, the 3D σ-NEB calculations did not converge at lower shear stresses giving higher E_a values. In addition to the activation energy, we determined the activation volume, defined as $V_\mathrm{a} = -\partial E_\mathrm{a}/\partial\tau$ [35]. Fig. 4d shows the V_a versus E_a curve (black solid line) derived from the E_a versus τ plot in Fig. 4c, with extrapolation to higher activation energies (indicated by the red dashed line). For $E_\mathrm{a} = 0.7$ eV, V_a is approximately $110 b_\mathrm{L}^3$ (star in Fig. 4d), where b_L is the Burgers vector length of a lattice dislocation in FCC Ni. These atomistically determined activation volumes can be compared with experimental measurements [36] to evaluate strain rate sensitivity and identify the rate-limiting process in polycrystals under typical laboratory strain rate conditions (~10^{-3} s^{-1}) . Such a comparison requires further model development to account for intragranular deformation processes, thereby bridging the gap between

activation volumes derived from bulk polycrystal experiments and those associated with local GB-mediated events [37]. Although the sliding direction examined here is consistent with that used in the in situ experiments, sliding in the reverse direction exhibits a modestly different athermal stress. This direction asymmetry warrants further investigation.

3. Discussion

3.1 GB misfit partial dislocations

To investigate the structure of coexisting partials of a secondary GB misfit dislocation, we sequentially introduced two such partials into a GB without preexisting secondary misfit dislocations, as shown in Fig. 5a. First, we imposed a locally controlled shift [34] of $\mathbf{b}_p$ across the boundary on the left side of the intended partial dislocation core, followed by structural relaxation (Fig. 5b). Subsequently, we increased the applied shear stress to displace this partial to the right end of the bicrystal (Fig. 5c). Next, we imposed a locally controlled shift of $\mathbf{b}_p$ across the boundary on the left side of the second intended partial dislocation core, followed by structural relaxation (Fig. 5d). Because the two partials possess identical partial Burgers vectors and therefore repel one another, a longer GB than that in Fig. 1a is required. The corresponding bicrystal measures 33 × 18 × 1 nm^3 and contains 55,252 atoms. This procedure can be extended to introduce four partials along a longer boundary, thereby reconstructing a complete secondary GB misfit dislocation. Alternatively, relaxation of an extended GB can result in multiple coexisting secondary GB misfit partials, as shown in Section 3.2.

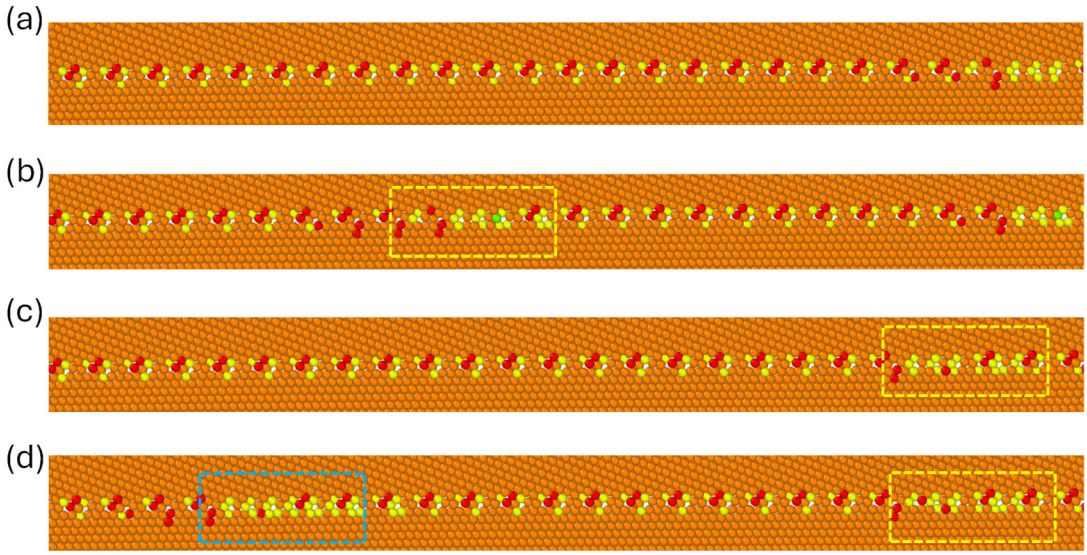

Fig. 5. Nonuniform sliding of an asymmetric ⟨110⟩ tilt GB with a 21.8° misorientation (same structure as Fig. 1a) via the sequential glide of two partials of a secondary GB misfit dislocation. Atoms are colored by coordination number, as in Fig. 2e. (a) Initial GB structure prior to sliding, with no secondary GB misfit dislocations present. (b) The first partial of a secondary GB misfit dislocation with $\mathbf{b}_p$ is introduced as the bicrystal is subjected to applied shear stress; the core of this partial is highlighted with a yellow box. (c) The first partial glides rightward under increasing shear stress. (d) The second partial with $\mathbf{b}_p$ is introduced under a further increase in shear stress; its core is marked with a blue box.

For the representative {331}/{111} GB, the structure-preserving translation **b** is accommodated by four successive partial translations of $\mathbf{b}_p = \mathbf{b}/4$. The dissociation into four partials reflects the specific sequence of intermediate translation states identified along the uniform-sliding pathway in Fig. 2. We emphasize that the detailed dissociation pattern is specific to this boundary and is not a universal feature of asymmetric non-CSL GBs. Other bicrystallographic configurations can exhibit different numbers, Burgers vectors, and core structures of GB misfit partial dislocations. Nevertheless, the broader description of a secondary GB misfit dislocation as a localized carrier of a structure-preserving interfacial translation remains applicable.

3.2 Near-CSL GB and misfit dislocations

The structural periodicity **λ** of the asymmetric non-CSL tilt GB in Fig. 1b suggests the existence of a near-CSL structure. Conventional CSL GBs are defined by exact coincidence sites in a dichromatic pattern formed by two rigid grains at a prescribed misorientation [6]. Here, we extend this framework to asymmetric non-CSL tilt GBs using the near-CSL scheme [38]. A near-CSL structure is identified by allowing a positional tolerance ($\sim 5\% b_L$), thereby accounting for the local atomic relaxation that occurs during GB formation. As illustrated in Fig. 6a, the dichromatic map for the bicrystal in Fig. 1a contains a diamond-shaped near-CSL motif outlined by pink lines. Boundary planes aligned with a diagonal or edge of this motif retain structural periodicity. Specifically, the vertical and horizontal diagonals correspond to mirror planes for symmetric GBs with the same misorientation, while the yellow edge defines the asymmetric GB plane analyzed in Fig. 1a. Along this edge, the {331} surface of grain G1 comprises four single-atom-height steps separated by short {111} facets and interfaces with the close-packed {111} surface of grain G2. This geometry produces a repeating motif containing four pentagon units, consistent with Fig. 1g. The near-CSL scheme therefore enables the construction of periodic structural units for complex

non-CSL tilt GBs. The source code for near-CSL analysis of dichromatic patterns is available on GitHub (https://github.com/Yazhuo-Liu/DichromaticMap).

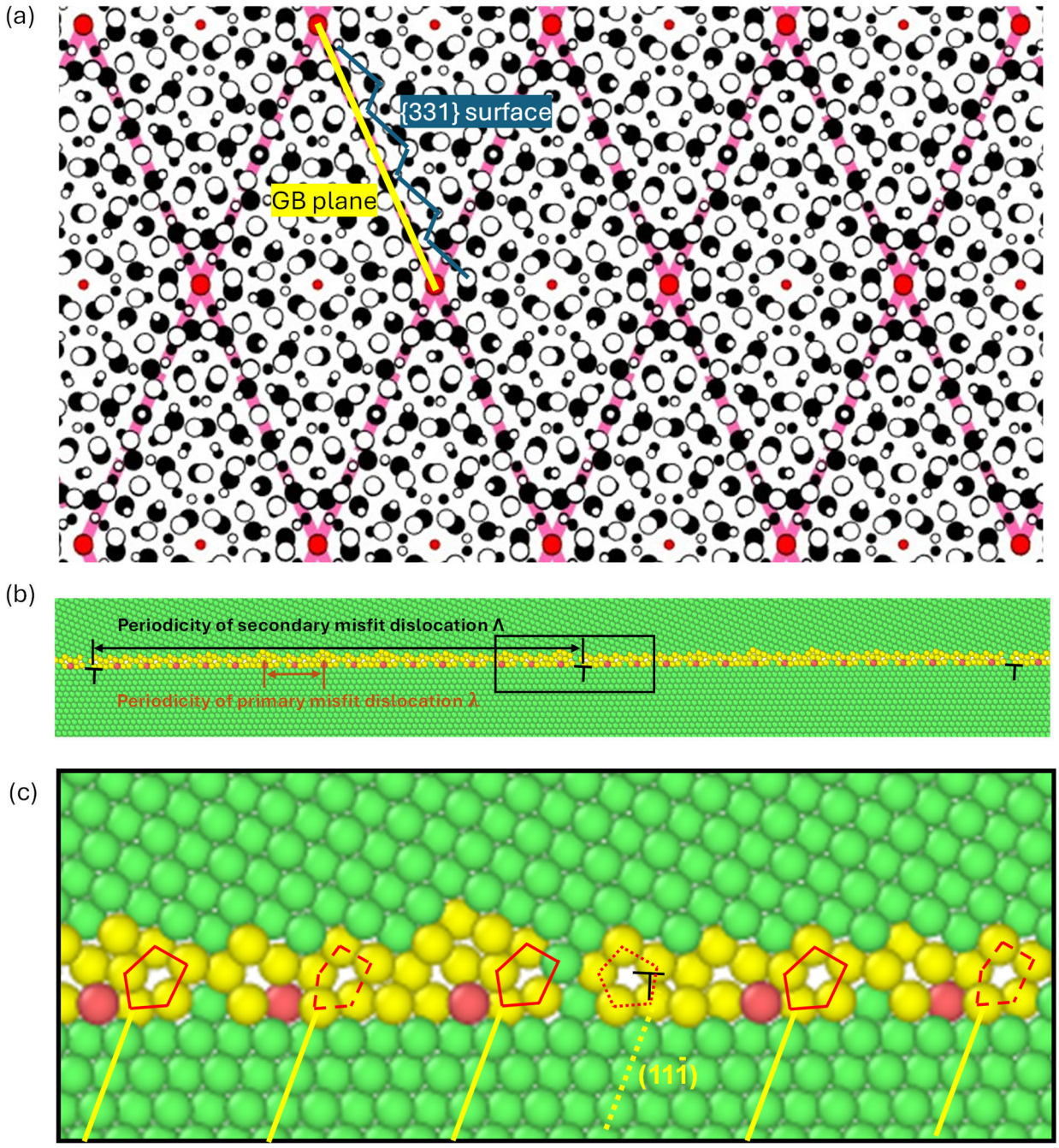

Fig. 6. Near-CSL analysis and long-range defect structure of the asymmetric {331}/{111} GB. (a) Dichromatic map of the bicrystal in Fig. 1a, revealing a near-CSL ($\sum 40$) motif characterized by a diamond-shaped pattern outlined in pink. GB planes aligned with the edges (thick red lines) of the diamond pattern preserve the periodic structure. The yellow edge defines the GB plane in Fig. 1a, where the {331} grain surface interfaces with the close-packed {111} grain surface. The {331}

surface consists of four single-atom-height steps separated by narrow {111} facets (marked in blue). (b) Atomic configuration of an extended GB. The short structural period $\lambda \sim 2.2$ nm corresponds to the repeated near-CSL structural unit, whereas the black $\perp$ symbols mark secondary misfit partial dislocations that accommodate the residual interface mismatch between the actual non-CSL boundary and the near-CSL reference. Their spacing exhibits a long period $\boldsymbol{\Lambda}$ with the average value of 16.2 nm. The black box indicates the region enlarged in (c). (c) Magnified atomic structure of a secondary misfit dislocation in (b). Its core is outlined by a yellow dotted pentagon, and the associated extra half-plane is marked by a yellow dotted line. Neighboring primary misfit dislocation cores are outlined by solid and dashed pentagons, with their extra half-planes marked by yellow solid lines. (b) and (c) are colored according to common neighbor analysis.

The near-CSL description also clarifies the relationship between asymmetric non-CSL GBs and conventional CSL GBs. A symmetric CSL tilt GB can often be represented by a periodic array of primary misorientation dislocations. No primary misfit component arises because the terminating grain planes are related by symmetry. By contrast, an asymmetric CSL tilt GB can contain two primary GB dislocation sets. One set accommodates lattice misorientation, whereas the other accommodates the mismatch between unequal terminating grain planes. The periodic arrangement of these dislocations defines the elementary boundary unit and its characteristic period. As the grain misorientation increases, the misorientation dislocations overlap and become difficult to resolve individually. However, primary misfit dislocations can remain identifiable from the disregistry between aligned close-packed atomic rows across the boundary. Because an exact CSL boundary is commensurate, no secondary GB misfit-dislocation array is required.

The asymmetric non-CSL GBs considered here are incommensurate. A near-CSL reference comprising primary GB misfit dislocations with repeat distance $\boldsymbol{\lambda}$ therefore cannot fully accommodate the lattice mismatch across the actual interface. The remaining mismatch is accommodated by secondary GB misfit dislocations, which appear as partial dislocations in the relaxed extended boundary. Consequently, the boundary exhibits two characteristic length scales. The short period $\boldsymbol{\lambda}$ is the repeat distance between neighboring equivalent primary GB misfit dislocations, which accommodate the local mismatch between adjoining grains. The long period $\boldsymbol{\Lambda}$ is the characteristic spacing between secondary GB misfit partial dislocations, which accommodate the residual mismatch relative to the near-CSL reference. In the finite-length GB considered here, $\boldsymbol{\lambda}$ and $\boldsymbol{\Lambda}$ should be interpreted as characteristic spacings associated with a rational approximation to the incommensurate boundary rather than as exact periodicities of an infinite

boundary. The value of $\mathbf{\Lambda}$ is governed by the residual mismatch and can also depend on the system geometry and boundary conditions.

The two characteristic length scales are illustrated in Fig. 6b for a relaxed, extended {331}/{111} boundary. The red atoms correspond to the cores of primary misfit dislocations, and the distance between every other red atom is $\lambda \sim 2.2$ nm. The secondary GB misfit partials are marked by black $\perp$ symbols and recur with an average spacing of 16.2 nm, corresponding to $\mathbf{\Lambda}$. Fig. 6c enlarges the boxed region in Fig. 6b and shows a secondary misfit partial. Its core is outlined by a dotted pentagon, and its associated extra half-plane is marked by a yellow dotted line. The neighboring primary misfit dislocation cores are outlined by solid and dashed pentagons, as in Fig. 1b, and their extra half-planes are marked by yellow solid lines. In regions containing only primary misfit dislocations, adjacent yellow solid lines are separated by four $(11\bar{1})$ atomic planes. Around the secondary misfit dislocation, the yellow dotted line is separated from each neighboring solid line by three $(11\bar{1})$ atomic planes. Hence, the dotted pentagon is located between two solid-outlined pentagons that are separated by six $(11\bar{1})$ atomic planes when the dotted extra half-plane is excluded from the count. This three-pentagon arrangement is consistent with the HRTEM observation in Fig. 4C of Ref. [8]. In addition, the local distribution of atomic coordination numbers around the secondary misfit partial differs from that around the neighboring primary misfit dislocations. Burgers vector analysis shows that this defect has the same Burgers vector as the shear-induced secondary misfit partial examined in Fig. 5. The similarity of their core structures provides additional support for this correspondence. The secondary misfit partials formed during relaxation of an extended GB therefore have the same crystallographic defect character as the glissile secondary GB misfit partials induced by shear loading in Fig. 5. The present work focuses on shear stress driven sliding associated with the repeating near-CSL structural units and a small number of secondary misfit partials in relatively short GBs. The collective interactions among multiple secondary GB misfit partials under shear remain for future study.

3.3 {111}/{100} GB

For asymmetric tilt GBs with larger misorientations, resolving individual GB misorientation dislocations becomes increasingly difficult. Nevertheless, the interfacial misfit component can still be identified from the atomic disregistry across the boundary. For example, we examined a high-

angle asymmetric $\langle 110 \rangle$ tilt GB previously characterized experimentally by Tian et al. [9]. This boundary has a structure similar to that shown in Figs. 1d-1f but has a larger misorientation angle of 54.7°. Based on the experimental structure, we constructed a corresponding GB model in a Ni bicrystal (Fig. 7a). Both grains are aligned along the $[\bar{1}10]$ zone axis. Grain G1 terminates at a low-index (001) surface, whereas grain G2 terminates at a flat close-packed (111) surface. The bicrystal measures 13 × 18 × 1 nm^3 and contains 22,079 atoms. As shown in Fig. 7b, primary misfit dislocations can be identified from the interfacial disregistry. Their repeating arrangement defines the structural periodicity $\boldsymbol{\lambda} = 2[\bar{1}\bar{1}2](111)$ relative to the G2 lattice (Figs. 7b-7d), which differs from the {331}/{111} boundary in Fig. 1b. By contrast, the larger misorientation angle prevents the misorientation component from being resolved as a discrete array of individually identifiable dislocations.

We next tested whether the structure-preserving slip vector changes when the misorientation and terminating plane of G1 are altered while G2 retains a flat (111) surface. Uniform-sliding calculations for the model in Fig. 7 give $\mathbf{b} = 1/2\langle 112 \rangle\{111\}$ relative to the G2 lattice. This DSC translation is completed through four sequential sliding steps (Figs. 7c1-7c5). During each increment, the average relative displacement within each structural period is approximately $\mathbf{b}/4 = 1/8\langle 112 \rangle\{111\}$, corresponding to the Burgers vector of the secondary GB misfit partials $\mathbf{b}_p$. The configurations in Figs. 7d0-7d4 show that not all G1 surface atoms occupy ideal three-fold hollow sites above the close-packed G2 surface. However, these local structural deviations do not alter the net slip vector. This comparison indicates that variations in misorientation and the opposing terminating plane can alter $\boldsymbol{\lambda}$ without changing $\mathbf{b}$ and $\mathbf{b}_p$, provided that the close-packed {111} surface is retained.

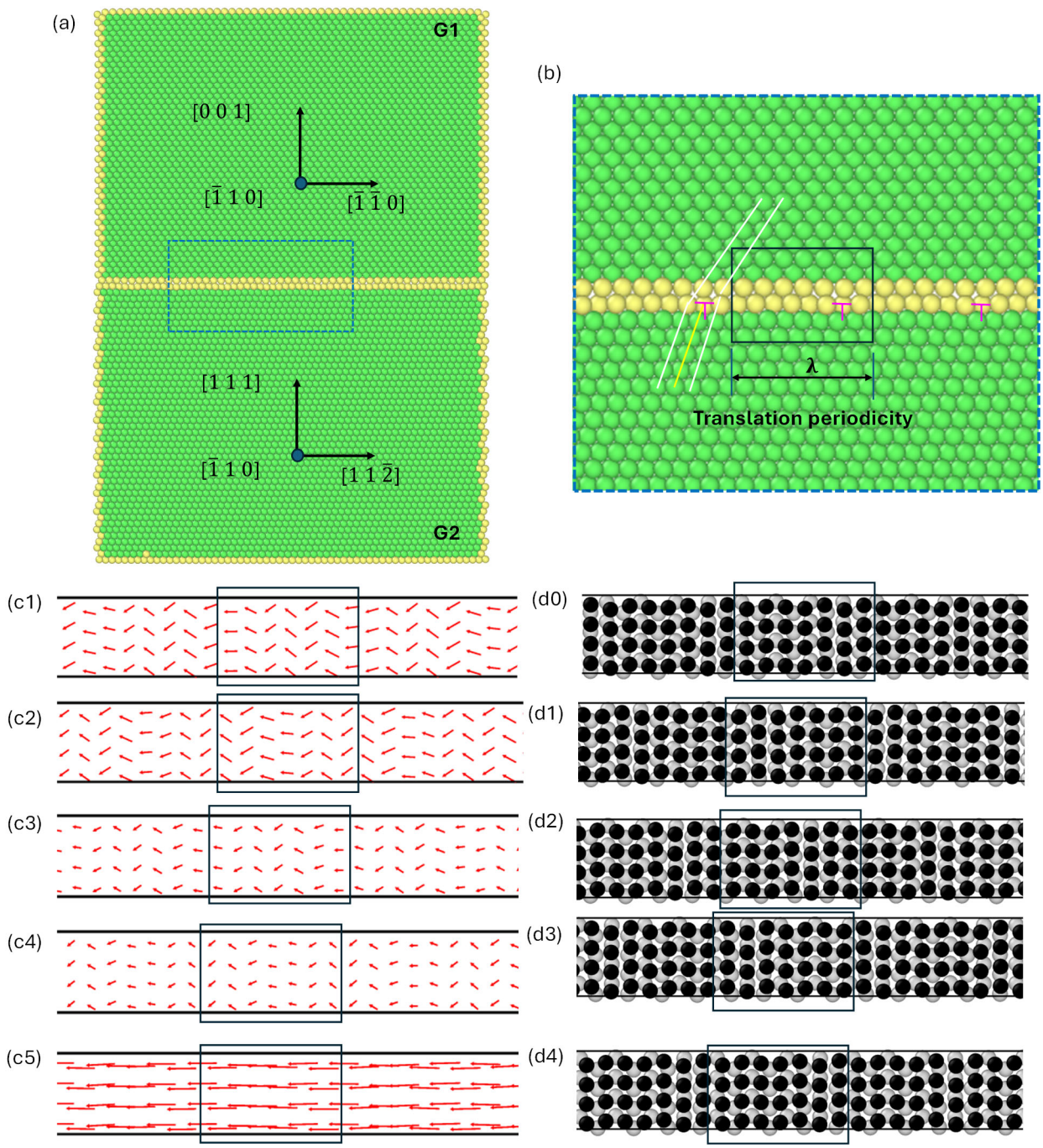

Fig. 7. {100}/{111} GB: an asymmetric ⟨110⟩ tilt GB with a 54.7° misorientation. (a) Atomic configuration of a Ni bicrystal: grain G1 exposes a (001) surface, while grain G2 exposes a close-packed (111) surface. (b) Enlarged view of the boxed region in (a). Primary misfit dislocations (marked by pink ⊥ symbols) are identified by terminations of an extra half-plane, highlighted by the yellow line. The structural periodicity λ is marked by the solid box. (c) Top-down relative displacement maps for nearest-neighbor atom pairs across the GB during four sequential sliding steps (c1-c4). (c5) shows the cumulative relative displacement map (sum of c1-c4). (d) Top-down

positions of G1 and G2 grain surface atoms before and after each of the four sequential sliding steps.

3.4 {100}/{110} GB

The above two GBs both contain a {111} terminating plane. We further examined whether the sliding characteristics **λ, b** and $\mathbf{b}_p$ depend on the presence of the close-packed {111} plane in FCC crystals. We constructed a crystallographically distinct asymmetric ⟨110⟩ tilt GB with a 90° misorientation between {100} and {110} terminating planes. As shown in Fig. 8a, grain G1 terminates at a $(\bar{1}\bar{1}0)$ surface, whereas grain G2 terminates at a (001) surface. The simulated GB structure agrees with the direct TEM observations reported by Gautam et al. [24]. This configuration differs substantially from the {331}/{111} and {100}/{111} boundaries considered above. Despite its distinct bicrystallography, the {100}/{110} GB exhibits a well-defined structural period **λ**, as shown in Fig. 8b. The terminations of extra half-planes identify a set of primary misfit dislocations whose arrangement repeats over **λ**. This result further supports the conclusion that the GB periodicity is determined by the repeating arrangement of primary misfit dislocations. The detailed dislocation arrangement differs from those of the {331}/{111} and {100}/{111} boundaries because of the different bicrystallography.

We next examined uniform sliding of the {100}/{110} GB. Figs. 8c1–8c3 show relative-displacement maps for nearest-neighbor atom pairs across the GB during three successive sliding increments, and Fig. 8c4 shows the cumulative displacement. The corresponding atomic configurations before and after each increment are presented in Figs. 8d0–8d3. After the third increment, the atomic arrangement within the marked periodic unit returns to a crystallographically equivalent configuration, indicating the completion of a DSC translation. The cumulative displacement in Fig. 8c4 gives $\mathbf{b} = 1/2\,[\bar{1}\bar{1}0](001)$, whereas the boundary period is $\boldsymbol{\lambda} = 17/2[\bar{1}\bar{1}0](001)$, with both quantities referenced to the G2 lattice. In Figs. 8c1-8c3, the average relative displacement within each structural period is approximately $\mathbf{b}/3 = 1/6[\bar{1}\bar{1}0](001)$, corresponding to the partial slip vector $\mathbf{b}_p$ in this boundary.

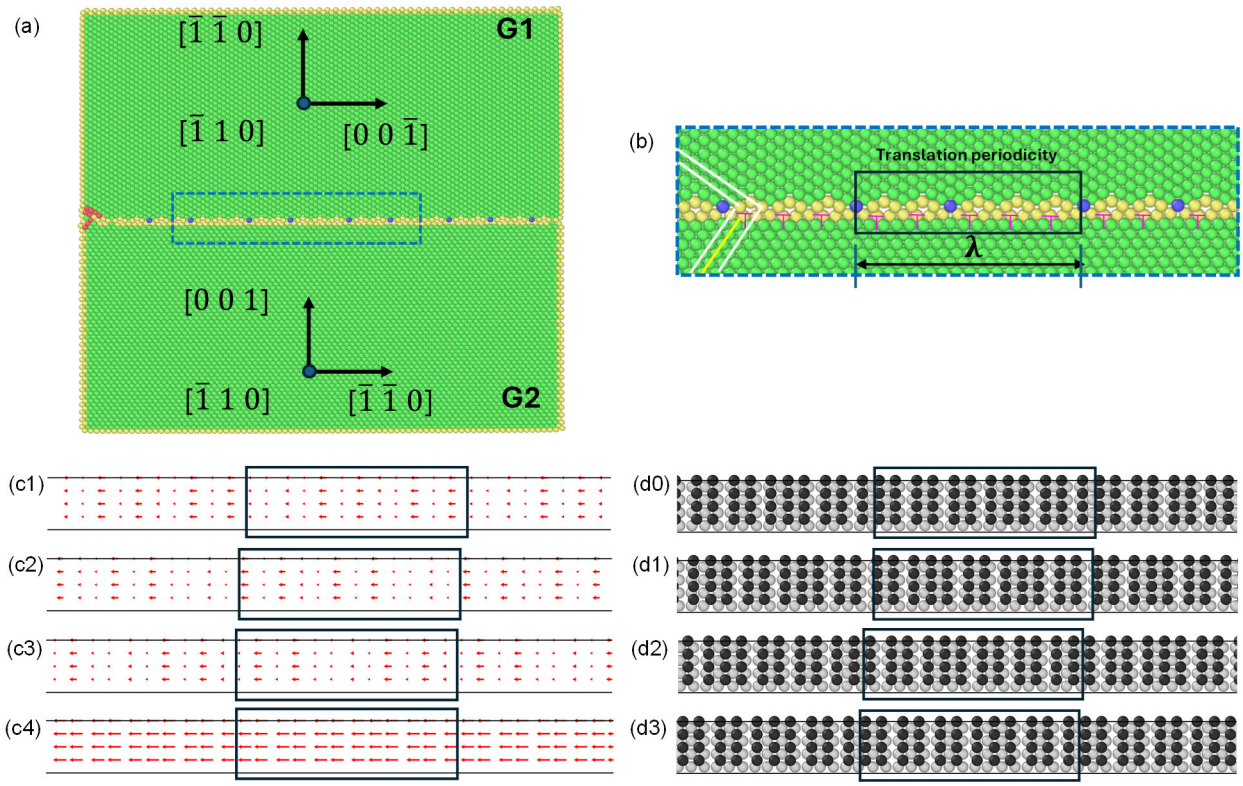

Fig. 8. {100}/{110} GB: an asymmetric ⟨110⟩ tilt GB with a 90° misorientation. (a) Atomic configuration of a Ni bicrystal: grain G1 terminates at a ($\bar{1}\bar{1}$0) surface, while grain G2 terminates at a relatively close-packed (001) surface. (b) Enlarged view of the dashed boxed region in (a). Primary misfit GB dislocations (pink ⊥ symbols) are identified by terminations of an extra half-plane (yellow line) of primary misfit dislocations. The corresponding structural period is marked by the solid box. (c) Top-down relative displacement maps for nearest-neighbor atom pairs across the GB during three sequential sliding steps (c1-c3). (c4) shows the cumulative relative displacement map (sum of c1-c3). (d) Top-down positions of G1 and G2 grain surface atoms before and after each of the three sequential sliding steps.

The sliding characteristics **λ**, **b** and $\mathbf{b}_p$ are therefore not universal among asymmetric non-CSL ⟨110⟩ tilt GBs. The with {111}-terminated GBs in Figs. 2 and 7 share a 1/2⟨112⟩{111} type slip vector but have different structural periods of 5/2⟨112⟩{111} and 2⟨112⟩{111}, respectively. By contrast, the {100}/{110} GB in Fig. 8 has **b** = 1/2⟨110⟩{100} and **λ** = 17/2⟨110⟩{100}. These results imply that **b** and the associated $\mathbf{b}_p$ are governed primarily by the lattice periodicity of the terminating plane with the higher planar atomic density. In contrast, **λ** remains associated with the repeating arrangement of primary misfit dislocations and therefore depends on the complete

bicrystallography. The {100}/{110} GB demonstrates that structure-preserving sliding mediated by GB misfit dislocations is not restricted to boundaries containing a {111}-terminating plane.

These results also distinguish the crystallographic characteristics of the sliding mode from material-dependent atomistic details. The existence of structure-preserving interfacial translation states and the slip values of $\boldsymbol{\lambda}$, $\mathbf{b}$ and $\mathbf{b}_p$ are determined primarily by bicrystallography. By contrast, the core structures of secondary GB misfit partials, the critical stress, the activation energy and activation volume of kink pairs depend on the interatomic interactions. The quantitative kinetic results should therefore be regarded as predictions for the present Ni model rather than direct quantitative predictions for the Pt experiments [8]. The Pt experiments provide the structural and mechanistic motivation for studying GB-dislocation-mediated sliding, whereas the Ni calculations reproduce the relevant experimental GB structural motifs and resolve the underlying crystallographic and atomistic mechanisms.

4. Concluding remarks

We investigated stress-driven sliding of asymmetric non-CSL GBs in FCC Ni using molecular statics and NEB calculations. Motivated by atomic-resolution experimental observations, we examined asymmetric ⟨110⟩ tilt GBs containing at least one low-index terminating plane, including {331}/{111}, {100}/{111} and {100}/{110}. The principal finding is that a misfit-dislocation hierarchy governs sliding of asymmetric non-CSL GBs. The supporting results are summarized below.

- Uniform sliding calculations reveal discrete structure-preserving interfacial translation states and identify two characteristic quantities. The smallest GB structural periodicity $\boldsymbol{\lambda}$ is defined by the repeating arrangement of primary GB misfit dislocations. The slip vector $\mathbf{b}$ is determined by the minimum DSC translation that restores an equivalent GB structure. Both quantities arise from bicrystallography but characterize distinct aspects of the interface. The calculations provide a systematic procedure for determining $\boldsymbol{\lambda}$ and $\mathbf{b}$.
- The extended asymmetric non-CSL GBs examined here are incommensurate [22] and contain two classes of misfit dislocations that accommodate distinct components of interfacial mismatch. Primary misfit dislocations accommodate the local mismatch, whereas secondary GB misfit dislocations accommodate the residual mismatch relative to

a near-CSL reference structure. A secondary misfit dislocation dissociates into partials with Burgers vector $\mathbf{b}_p$. The characteristic spacing between its partials defines a longer length scale $\boldsymbol{\Lambda}$.

- Nonuniform sliding is mediated by secondary misfit dislocations. Primary misfit dislocations undergo only local positional rearrangements and do not propagate over distances exceeding $\boldsymbol{\lambda}$. They are therefore effectively non-glissile within the GB plane. By contrast, secondary misfit dislocations are glissile over distances substantially greater than $\boldsymbol{\lambda}$ and carry the structure-preserving translation $\mathbf{b}$.
- For the representative {331}/{111} GB, a secondary GB misfit dislocation dissociates into four partials. The Burgers vectors of the full secondary misfit dislocation and its constituent partials, $\mathbf{b}$ and $\mathbf{b}_p$, are $1/2\langle 112\rangle\{111\}$ and $1/8\langle 112\rangle\{111\}$, respectively. The short structural period λ and the longer period Λ are 2.2 nm and 16.2 nm, respectively. The thermally activated propagation of a partial proceeds through localized kink-pair formation and migration. Each elementary propagation event comprises two sequential steps, each advancing the partial by $\lambda/2$, for a total advance of λ. Secondary GB misfit dislocations also dissociate into four and three partials in the {100}/{111} and {100}/{110} GBs, respectively.

Several directions remain for future research. The present study considered asymmetric tilt GBs containing at least one low-index terminating plane. General GBs can exhibit pronounced interface-energy anisotropy with respect to boundary inclination and may reduce interfacial energy by faceting into locally favorable orientations. Low-index and close-packed planes therefore frequently form constituent facets of general asymmetric GBs. The framework developed here can be extended to analyze sliding along such faceted interfaces. Furthermore, this study does not systematically compare the sliding resistance of different GBs. Quantifying these resistances is necessary to determine how GB sliding competes with other intergranular and intragranular deformation mechanisms in polycrystals. In addition, the effects of shear loading on interactions between distributed secondary GB misfit partials remain for future study. More broadly, because GB sliding and interfacial friction both involve relative motion between adjoining lattices, the present results provide insight into friction between incommensurate crystals [22]. Overall, this work establishes a unified crystallographic and dislocation-based framework for understanding stress-driven sliding in structurally complex asymmetric GBs.

References

[1] A.P. Sutton, R.W. Balluffi, Interfaces in Crystalline Materials Oxford University Press, Oxford, UK, 1995.

[2] T. Zhu, J. Li, Ultra-strength Materials, Progress in Materials Science 55 (2010) 710-757.

[3] M.F. Ashby, Boundary defects, and atomistic aspects of boundary sliding and diffusional creep, Surface Science 31 (1972) 498-542.

[4] J.W. Cahn, Y. Mishin, A. Suzuki, Coupling grain boundary motion to shear deformation, Acta Materialia 54 (2006) 4953-4975.

[5] D.L. Medlin, K. Hattar, J.A. Zimmerman, F. Abdeljawad, S.M. Foiles, Defect character at grain boundary facet junctions: Analysis of an asymmetric $\Sigma = 5$ grain boundary in Fe, Acta Materialia 124 (2017) 383-396.

[6] J. Han, S.L. Thomas, D.J. Srolovitz, Grain-boundary kinetics: A unified approach, Progress in Materials Science 98 (2018) 386-476.

[7] T. Meiners, T. Frolov, R.E. Rudd, G. Dehm, C.H. Liebscher, Observations of grain-boundary phase transformations in an elemental metal, Nature 579 (2020) 375-378.

[8] L. Wang, Y. Zhang, Z. Zeng, H. Zhou, J. He, P. Liu, M. Chen, J. Han, D.J. Srolovitz, J. Teng, Y. Guo, G. Yang, D. Kong, E. Ma, Y. Hu, B. Yin, X. Huang, Z. Zhang, T. Zhu, X. Han, Tracking the sliding of grain boundaries at the atomic scale, Science 375 (2022) 1261-1265.

[9] Y. Tian, X. Gong, M. Xu, C. Qiu, Y. Han, Y. Bi, L.V. Estrada, E. Boltynjuk, H. Hahn, J. Han, D.J. Srolovitz, X. Pan, Grain rotation mechanisms in nanocrystalline materials: Multiscale observations in Pt thin films, Science 386 (2024) 49-54.

[10] R. Dang, Y.-W. Zhang, H. Gao, Predicting shear coupling behaviors in disconnection-mediated migration of asymmetrical tilt grain boundaries, International Journal of Plasticity 193 (2025) 104441.

[11] H. Grimmer, W. Bollmann, D.H. Warrington, Coincidence-site lattices and complete pattern-shift in cubic crystals, Acta Crystallographica Section A 30 (1974) 197-207.

[12] Z.T. Trautt, A. Adland, A. Karma, Y. Mishin, Coupled motion of asymmetrical tilt grain boundaries: Molecular dynamics and phase field crystal simulations, Acta Materialia 60 (2012) 6528-6546.

[13] D.E. Spearot, M.A. Tschopp, K.I. Jacob, D.L. McDowell, Tensile strength of 〈100〉 and 〈110〉 tilt bicrystal copper interfaces, Acta Materialia 55 (2007) 705-714.

[14] M. Wagih, C.A. Schuh, Viewpoint: Can symmetric tilt grain boundaries represent polycrystals?, Scripta Materialia 237 (2023) 115716.

[15] H.A. Khater, A. Serra, R.C. Pond, J.P. Hirth, The disconnection mechanism of coupled migration and shear at grain boundaries, Acta Materialia 60 (2012) 2007-2020.

[16] M.L. Bowers, C. Ophus, A. Gautam, F. Lançon, U. Dahmen, Step coalescence by collective motion at an incommensurate grain boundary, Physical Review Letters 116 (2016) 106102.

[17] Q. Zhu, G. Cao, J. Wang, C. Deng, J. Li, Z. Zhang, S.X. Mao, In situ atomistic observation of disconnection-mediated grain boundary migration, Nature Communications 10 (2019) 156.

[18] D.L. Medlin, S.M. Foiles, D. Cohen, A dislocation-based description of grain boundary dissociation: application to a 90° 〈110〉 tilt boundary in gold, Acta Materialia 49 (2001) 3689-3697.

[19] K.L. Merkle, L.J. Thompson, F. Phillipp, In-Situ HREM Studies of Grain Boundary Migration, Interface Science 12 (2004) 277-292.

[20] O. Hardouin Duparc, J.-P. Couzinié, J. Thibault-Pénisson, S. Lartigue-Korinek, B. Décamps, L. Priester, Atomic structures of symmetrical and asymmetrical facets in a near Σ=9{221} tilt grain boundary in copper, Acta Materialia 55 (2007) 1791-1800.
[21] R.C. Pond, D.L. Medlin, A. Serra, A study of the accommodation of coherency strain by interfacial defects at a grain boundary in gold, Philosophical Magazine 86 (2006) 4667-4684.
[22] J. Friedel, P.G. de Gennes, Friction between incommensurate crystals, Philosophical Magazine 87 (2007) 39-49.
[23] F. Lançon, J.M. Pénisson, U. Dahmen, Quasicrystalline gold interface with a hypo-friction property, Europhysics Letters 49 (2000) 603.
[24] A. Gautam, C. Ophus, F. Lançon, V. Radmilovic, U. Dahmen, Atomic structure characterization of an incommensurate grain boundary, Acta Materialia 61 (2013) 5078-5086.
[25] F. Lançon, J. Ye, D. Caliste, T. Radetic, A.M. Minor, U. Dahmen, Superglide at an Internal Incommensurate Boundary, Nano Letters 10 (2010) 695-700.
[26] X.Y. Li, Z.H. Jin, X. Zhou, K. Lu, Constrained minimal-interface structures in polycrystalline copper with extremely fine grains, Science 370 (2020) 831-836.
[27] W. Xu, B. Zhang, K. Du, X.Y. Li, K. Lu, Thermally stable nanostructured Al-Mg alloy with relaxed grain boundaries, Acta Materialia 226 (2022) 117640.
[28] H. Fu, X. Zhou, Z. Gao, Z. Jin, X. Li, K. Lu, Effect of Grain Geometry on the Stability of Polycrystalline Pt at the Nanoscale, Physical Review Letters 134 (2025) 056101.
[29] Y. Chen, J. Han, H. Deng, G. Cao, Z. Zhang, Q. Zhu, H. Zhou, D.J. Srolovitz, J. Wang, Revealing grain boundary kinetics in three-dimensional space, Acta Materialia 268 (2024) 119717.
[30] S. Plimpton, Fast parallel algorithms for short-range molecular dynamics, Journal of Computational Physics 117 (1995) 1-19.
[31] A. Stukowski, Visualization and analysis of atomistic simulation data with OVITO–the Open Visualization Tool, Modelling and Simulation in Materials Science and Engineering 18 (2010) 015012.
[32] C.A. Howells, Y. Mishin, Angular-dependent interatomic potential for the binary Ni–Cr system, Modelling and Simulation in Materials Science and Engineering 26 (2018) 085008.
[33] Y. Si, Y. Zhang, D. Chen, J.L. Wormald, B.S. Anglin, D.L. McDowell, T. Zhu, Atomistic determination of Peierls barriers of dislocation glide in nickel, Journal of the Mechanics and Physics of Solids 178 (2023) 105359.
[34] T. Zhu, J. Li, A. Samanta, H.G. Kim, S. Suresh, Interfacial plasticity governs strain rate sensitivity and ductility in nanostructured metals, Proceedings of the National Academy of Sciences of the USA 104 (2007) 3031-3036.
[35] Y. Zhang, K. Ding, S. Stangebye, D. Chen, J. Kacher, O. Pierron, T. Zhu, Atomistic modeling of surface and grain boundary dislocation nucleation in FCC metals, Acta Materialia 237 (2022) 118155.
[36] S. Gupta, S. Stangebye, K. Jungjohann, B. Boyce, T. Zhu, J. Kacher, O.N. Pierron, In situ TEM measurement of activation volume in ultrafine grained gold, Nanoscale 12 (2020) 7146-7158.
[37] H. Conrad, Plastic deformation kinetics in nanocrystalline FCC metals based on the pile-up of dislocations, Nanotechnology 18 (2007) 325701.
[38] R. Bonnet, E. Cousineau, D.H. Warrington, Determination of near-coincident cells for hexagonal crystals. Related DSC lattices, Acta Crystallographica A37 (1981) 184-189.